Journal of Colloid and Interface Science 590 (2021) 226–237

Contents lists available at ScienceDirect

Journal of Colloid and Interface Science

journal homepage: www.elsevier.com/locate/jcis

Regular Article

Synergistic effects of Fe and Mn dual-doping in Co_3S_4 ultrathin nanosheets for high-performance hybrid supercapacitors

Wen Lu [a,1], Ying Yang [a,1], Tianyu Zhang [b,1], Luankexin Ma [c], Xiting Luo [d], Chuanqi Huang [d,*], Jiqiang Ning [e], Yijun Zhong [a], Yong Hu [a,*]

[a] Key Laboratory of the Ministry of Education for Advanced Catalysis Materials, Department of Chemistry, Zhejiang Normal University, Jinhua 321004, China
[b] School of Biological and Medical Engineering, School of Food Science and Engineering, Hefei University of Technology, Hefei 230009, China
[c] Queen Mary University of London Engineering School, NPU/Material Science and Engineering, Northwestern Polytechnical University, Xian 710000, China
[d] Hangzhou Institute of Advanced Studies, Zhejiang Normal University, Hangzhou, Zhejiang 311231, China
[e] Vacuum Interconnected Nanotech Workstation, Suzhou Institute of Nano-Tech and Nano-Bionics, Chinese Academy of Sciences, Suzhou 215123, China

HIGHLIGHTS

- Dopant engineering is an effective strategy to enhance electrochemical performances.
- The FM-Co_3S_4 ultrathin NSAs are prepared via a hydrothermal method followed by a sulfurization reaction.
- FM-Co_3S_4 ultrathin NSAs with more electroactive sites show better specific capacity and rate capability.
- The assembled devices exhibit an energy density of 55 Wh kg^{-1} at the power density of 752 W kg^{-1}.

GRAPHICAL ABSTRACT

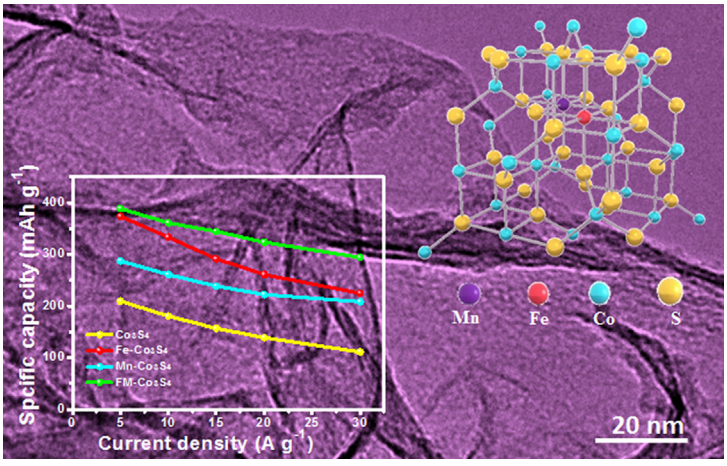

ARTICLE INFO

Article history:
Received 3 December 2020
Revised 15 January 2021
Accepted 16 January 2021
Available online 21 January 2021

Keywords:
Co_3S_4
Fe, Mn dual-doping
Ultrathin nanosheets
High specific capacity
Hybrid supercapacitors

ABSTRACT

Dopant engineering in nanostructured materials is an effective strategy to enhance electrochemical performances via regulating the electronic structures and achieving more active sites. In this work, a robust electrode based on Fe and Mn co-doped Co_3S_4 (FM-Co_3S_4) ultrathin nanosheet arrays (NSAs) on the Ni foam substrate is prepared through a facile hydrothermal method followed by a subsequent sulfurization reaction. It has been found that the incorporation of Fe ions is beneficial to higher specific capacity of the final electrode and Mn ions contribute to the excellent rate capability in the reversible redox processes. Density functional theory (DFT) calculations further verify that the Mn doping in the Co_3S_4 obviously shorten the energy gap of Co_3S_4, which favors the electrochemical performances. Due to the synergetic effects of different transition metal ions, the as-prepared FM-Co_3S_4 ultrathin NSAs exhibit a high specific capacity of 390 mAh g^{-1} at 5 A g^{-1}, as well as superior rate capability and excellent cycling stability. Moreover, the corresponding quasi-solid-state hybrid supercapacitors constructed with the FM-Co_3S_4 ultrathin NSAs and active carbon exhibit a high energy density of 55 Wh kg^{-1} at the power density of

* Corresponding authors.
E-mail addresses: hchuanqi@foxmail.com (C. Huang), yonghu@zjnu.edu.cn (Y. Hu).
[1] These authors contributed equally to this work.

https://doi.org/10.1016/j.jcis.2021.01.050
0021-9797/© 2021 Elsevier Inc. All rights reserved.

752 W kg^{-1}. These findings demonstrate a new platform for developing high-performance electrodes for energy storage applications.

© 2021 Elsevier Inc. All rights reserved.

1. Introduction

The ever-increasing demand for modern electronics has driven the development of the state-of-the-art energy storage devices [1,2]. Owing to the fast charging/discharging rates, excellent cycling life and high-power density, supercapacitors (SCs) have turned out to be promising candidates for energy storage devices and drawn wide attention from many various fields including digital cameras, portable devices and hybrid electric vehicles [3,4]. However, the problem of low energy densities drastically limits their practical applications [5]. Therefore, it is the key to further improve the energy density of SCs without sacrificing power density by the means of maximizing the specific capacities and cell voltages [6,7]. Generally, the development of advanced electrode materials is considered as a crucial way to achieve high specific capacity [8,9], and the construction of hybrid supercapacitors (HSCs) is an appropriate choice to widen the voltage window [10,11].

Recently, transition metal electrodes, especially Co-based materials, have been considered as promising candidates for SCs due to their low cost, high theoretical specific capacitance and excellent electroactivity [12–15]. Nevertheless, their electrochemical performances are still restricted by the poor rate capability and inferior stability caused by sluggish reaction kinetics [16,17]. It is promising to introduce different heteroatoms to form multi-composition Co-based materials for the aim of offsetting the drawbacks and enhance electrochemical performances [12,18,19]. Specifically, heteroatom doping into the Co-based materials tends to change the charge states [20,21], resulting in more electroactive sites and improved electrical conductivity to facilitate the reaction kinetics and optimize their intrinsic activity [22,23], and therefore superior rate capability, specific capacity and stability [24]. Moreover, the multi-composition Co-based materials integrate the advantages of constituent to achieve synergetic effects of the different ingredients [25–27]. For example, Huang and co-workers have synthesized CNVO 2D thin sheets, which display superior supercapacitor performance owing to well-defined porous morphology and synergistic contributions of the individual components [28]. Wang and co-workers have developed the system of ZnNiCo-P, which exhibits superior electrochemical performance to Co-P systems. It is well established that the incorporation of Zn and Ni into Co-P system can facilitate the utilization of electrons and increase the multiple valences of the cations, resulting in prominent electrochemical performances [29]. Huang and co-workers have prepared $Co_{0.5}Ni_{0.5}WO_4$ electrodes, which demonstrates significantly improved electrochemical property due to the unique 3D/2D porous nanostructures and synergistic effects [30]. Therefore, it is expected that regulating the electronic structures by tailoring the compositions can efficiently boost the electrochemical performances.

Structure-engineering with well-defined morphologies is another effective strategy to boost electrochemical performances [31–33]. Among various structural designs, two-dimensional (2D) nanosheet arrays (NSAs) with atomic thickness are featured with higher active surfaces, shorter carrier diffusion paths, superior intrinsic porosity, high electrical conductivity and excellent cycling stability, which endow them with the potential in energy storage applications [34–36]. In particular, the cross-linked ultrathin NSAs can not only provide abundant electroactive sites to accelerate the reaction kinetics [37], but also offer efficient voids to alleviate volume variation, resulting in excellent stability [38]. Zhu *et al.* demonstrated a facile synthesis of 2D porous Co_3O_4 thin sheets, revealing a high specific capacity and excellent rate performance [39]. Huang *et al.* synthesized porous 2D CoNi-LDH thin sheets with honeycomb-like nanostructure, which delivers excellent electrochemical properties [40]. Zhu *et al.* prepared $ZnCo_2O_4$ thin sheets, which show much improvements of energy density and cycling life [41]. Despite these advances achieved, the rational design of ultrathin NSAs with controllable compositions is still a challenge.

Herein, we have developed a facile strategy to prepare Fe and Mn co-doped Co_3S_4 (FM-Co_3S_4) ultrathin NSAs on the Ni foam substrate. In this strategy, the CoFeMn-precursors are first achieved through a facile hydrothermal and then transformed to FM-Co_3S_4 ultrathin NSAs via a sulfidation reaction. Compared with the pristine Co_3S_4 ultrathin NSAs, the doping of Fe and Mn into Co_3S_4 ultrathin NSAs can not only improve the electrical conductivity, but also introduce more electroactive sites to promote the reactions and optimize the overall activity for enhanced electrochemical performances. Specially, the effect of Fe or Mn doping on the electronic property of Co_3S_4 was further investigated by the density functional theory (DFT). The resulting data reveals a better electrical conductivity for charge transfer in Mn-Co_3S_4, providing a theoretical support for the experimental results. The FM-Co_3S_4 ultrathin NSAs integrate the advantages of the unique structure and synergistic effects of the components, which delivers a much higher specific capacity of 390 mA h g^{-1} at the current density of 5 A g^{-1} along with excellent rate capability and cycling stability. In addition, the constructed HSC device exhibits a high energy density of 55 Wh kg^{-1} at a power density of 752 W kg^{-1} and long-term cycling stability. The outstanding performances of FM-Co_3S_4 ultrathin NSAs render it a promising potential for next-generation energy storage or conversion applications.

2. Experimental section

2.1. Preparation of the CoFeMn-OH ultrathin NSAs

In a typical procedure, a piece of Ni foam (NF, 2 cm × 4 cm) was sonicated in 3 M HCl solution and then washed with deionized water and ethanol several times. 0.169 g $MnSO_4{\cdot}H_2O$, 0.278 g $FeSO_4{\cdot}7H_2O$, 0.562 g $CoSO_4{\cdot}7H_2O$, 0.841 g $C_6H_{12}N_4$ and 0.074 g NH_4F were dissolved in 40 mL distilled water under sonication for 10 min to obtain a clear solution. Then the treated NF and the solution were transferred into a 50 mL Teflon-lined stainless autoclave and maintained at 120 °C for 8 h. When cooled down to room temperature, the NF was washed with distilled water and ethanol several times and dried at 60 °C for 12 h.

2.2. Preparation of FM-Co_3S_4 ultrathin NSAs

The FM-Co_3S_4 ultrathin NSAs were prepared by a facile solvothermal method. Briefly, 0.18 g of thioacetamide (TAA) was dissolved in 40 mL ethanol to form homogeneous solution. The resulting solution was transferred into a 50 mL Teflon-lined stainless autoclave, and the CoFeMn-OH supported on NF was then put into the autoclave. After maintained at 120 °C for 4 h, the autoclave

was cooled to room temperature and the NF was washed with distilled water and ethanol several times and dried at 60 °C for 12 h.

2.3. Preparation of Mn-Co_3S_4 ultrathin NSAs

The synthesis procedure of Mn-Co_3S_4 ultrathin NSAs is similar to the synthesis of FM-Co_3S_4 ultrathin NSAs described above, except the usage of $FeSO_4{\cdot}7H_2O$.

2.4. Preparation of Fe-Co_3S_4 ultrathin NSAs

The synthesis procedure of Fe-Co_3S_4 ultrathin NSAs is similar to the synthesis of FM-Co_3S_4 ultrathin NSAs described above, except the usage of $MnSO_4{\cdot}H_2O$.

2.5. Preparation of Co_3S_4 ultrathin NSAs

The synthesis procedure of Mn-Co_3S_4 ultrathin NSAs is similar to the synthesis of FM-Co_3S_4 ultrathin NSAs described above, except the usage of $FeSO_4{\cdot}7H_2O$ and $MnSO_4{\cdot}H_2O$.

2.6. Characterization

The crystallographic information and phase purity of the samples were identified by powder X-ray diffraction (XRD) measurements (Bruker D8 Advance diffractometer with Cu-Kα radiation). The morphology and microstructure were examined by the technique of field-emission scanning electron microscopy (FESEM; Hitachi S-4800), TEM (JEOL JEM-2100F), and HRTEM. The surface compositions and oxidation states of the samples were examined by X-ray photoelectron spectroscopy (XPS; ESCALab MKII with Al Kα X-ray). Raman spectra were recorded on a Renishaw RM 1000 system with a laser line of 633 nm. The specific surface area and corresponding pore size distribution were determined on the Brunauer-Emmett-Teller (BET) technique by a gas adsorption instrument (Autosorb-IQ, Quantachrome).

2.7. Electrochemical measurements

The electrochemical performance was characterized by cyclic voltammetry (CV), galvanostatic charge–discharge (GCD) and electrochemical impedance spectroscopy (EIS) on a CHI 660E electrochemical workstation (Chenhua, Shanghai) in a three-electrode or two-electrode configuration. A typical three-electrode system was investigated in 6 M KOH, in which the Hg/HgO and Pt foil work as the reference electrode and counter electrode, respectively. EIS was performed at open circuit potential with the amplitude 5 mV in the frequency range from 100 kHz to 10 MHz.

The specific capacity (C_s, mAh g^{-1}) and specific capacitance (C_{sp}, F g^{-1}) of the electrodes in a half cell are calculated according to Eqs. (1) and (2),

$$C_S = \frac{2i\int V dt}{mV} \tag{1}$$

$$C_{sp} = \frac{I\Delta t}{m\Delta V} \tag{2}$$

where I represents the current (A), Δt means the discharge time (s), m refers to the mass of the active materials (g), and ΔV corresponds to the potential window (V), $\int V\,dt$ is the integral area under the discharge curve, respectively.

2.8. Assembly of quasi-solid-state HSCs

The quasi-solid-state HSCs were assembled with the FM-Co_3S_4 ultrathin NSAs and activated carbon (AC) as positive and negative electrodes, respectively, and poly(vinyl alcohol) (PVA)/KOH as the gel electrolyte. The PVA/KOH gel electrolyte was prepared by the following process. 3.0 g of PVA was dissolved in 20 mL of distilled water at 90 °C under vigorously stirring, and 10 mL of KOH solution (0.3 g/mL) was dropped in until the solution became clear. Then the electrodes were soaked in the gel for 10 min before assembling. Finally, the quasi-solid-state HSCs were wrapped with a Kapton film.

Prior to assemble HSCs, the mass ratio of the positive electrode to the negative electrode is decided according to the following Eq. (3),

$$\frac{m_+}{m_-} = \frac{C_-\Delta V_-}{C_+\Delta V_+} \tag{3}$$

where m is the loading mass of the active material (g), C is the specific capacitance (F g^{-1}), and ΔV is the potential (V) window range for the positive and negative electrodes, respectively.

Based on the equation, the mass ratio of the FM-Co_3S_4 ultrathin NSAs to AC is approximately 1:9 and the mass loading of FM-Co_3S_4 ultrathin NSAs and AC is about 1.5 mg and 13.5 mg, respectively. Therefore, the total mass loading of the assembled HSC is about 15 mg. The negative electrode was fabricated by pressing the mixture consisting of AC, carbon black and polyvinylidene-fluoride (PVDF) with the mass ratio of 8:1:1 in *N*-methylpyrrolidone (NMP) onto a NF and dried at 70 °C for 12 h in a vacuum oven.

The energy density E (Wh kg^{-1}) and power density P (W kg^{-1}) of the HSCs are determined with the following formulas:

$$E = \frac{1}{2}C\Delta V^2 \tag{4}$$

$$P = \frac{E}{t} \tag{5}$$

where C refers to the specific capacitance (F g^{-1}), ΔV represents the potential (V) window and t means the discharge time (s), respectively.

2.9. DFT calculations

DFT calculations were performed using Vienna ab initio Simulation Package (VASP) based on the projected augmented wave (PAW) method Spin-polarized Perdew-Burke-Ernzerhof (PBE) exchange-correlation functional and on-site Coulomb repulsion U term for d electrons in spirit of Hubbard via Dudarev's approach has been employed to describe exchange and correlation. Effective U values for 3d electron of Co, Fe and Mn were 5.9 eV, 3.8 eV and 4.0 eV, respectively, referring to previous studies. A plane wave basis set with energy cut off of 400 eV and appropriate k-points were used to ensure the convergence of total ground-state energy. All geometrical optimizations were performed until force acting on relaxing atoms was less than 0.02 eV/Å. The lattice constant of Co_3S_4 with conventional spinel cell was optimized to 9.67 Å. Doping configuration of Fe or Mn atom substituting one Co atom on octahedral site or tetrahedral site in a single conventional spinel cell were considered, thus the modeling doping ratio was 1/24 with respect to Co.

3. Results and discussion

The synthetic procedure of the FM-Co_3S_4 ultrathin NSAs is schematically illustrated in Fig. 1. Uniform CoFeMn-OH ultrathin NSAs on NF are first prepared through a facile hydrothermal method, which are then converted to FM-Co_3S_4 ultrathin NSAs by an anion-exchange reaction at 120 °C for 4 h. The morphology and structure of the as-prepared samples were analyzed by SEM image. The SEM images of CoFeMn-OH reveal that the ultrathin

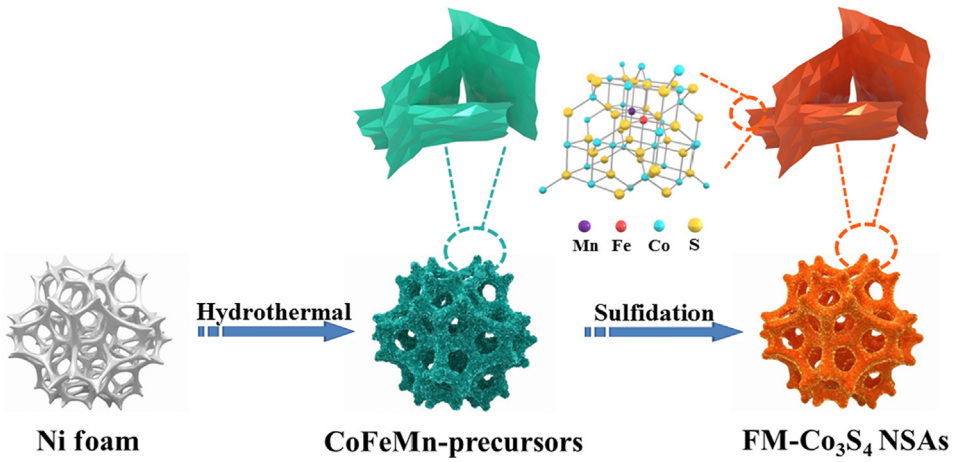

Fig. 1. Schematic illustration of the synthetic procedures of FM-Co_3S_4 ultrathin NSAs.

nanosheets are vertically grown on the NF, and the network consists of interconnected nanosheets with a smooth surface (Fig. 2a and b). As shown in Fig. S1a, the corresponding XRD pattern indicates the formation of CoFeMn-OH (JCPDS No. 50-0235). As a comparison, CoMn-LDH, CoFe-LDH and $Co(OH)_2$ ultrathin NSAs are also successfully synthesized without the addition of Fe source, Mn source and combined Mn and Fe sources, and the diffraction peaks can be identified as CoMn-LDH (JCPDS No. 46-0605), CoFe-LDH (JCPDS No. 50-0235) and $Co(OH)_2$ (JCPDS No. 02-0925), respectively (Fig. S2a, S3a and S4a). From the SEM images, it can be seen that the CoMn-LDH, CoFe-LDH and $Co(OH)_2$ have the similar nanosheet arrays (Fig. S2b, S3b and S4b). Meanwhile, the elemental compositions of the samples were explored via energy dispersive X-ray (EDX) analysis (Fig. S1b, S2c, S3c and S4c). It reveals that there is minor Fe and Mn in the as-obtained samples, which can be attributed that the higher solubility product constant of Mn-based and Fe-based hydroxides than Co-based hydroxides [42,43]. Meanwhile, the adsorption rate for Co^{2+} on Ni foam is faster than Fe^{2+} and Mn^{2+} due to their different ionic radius and ion mass [44,45]. After sulfidation, the CoFeMn-OH precursor are transformed into FM-Co_3S_4 ultrathin NSAs, which can be confirmed by the XRD analysis. The diffraction peaks of the FM-Co_3S_4 ultrathin NSAs can be well indexed to the Co_3S_4 ultrathin NSAs (JCPDS No. 47-1738), without any impurity phase of iron or manganese sulfate detectable, implying the achieved co-doping of Fe and Mn (Fig. 3). The successful formation of FM-Co_3S_4 ultrathin NSAs is also verified by Raman spectra. As shown in Fig. S5, the peaks located at 190, 467, 513 and 666 cm^{-1} are corresponding to the A_g, E_g, F_{2g} and A_{1g} modes of Co_3S_4, respectively [46–48]. Fig. 2c and d depict that the structure and morphology of the as-prepared FM-Co_3S_4 ultrathin NSAs are well inherited from the CoFeMn-OH precursor except the roughened surface. Fe-Co_3S_4 ultrathin NSAs, Mn-Co_3S_4 ultrathin NSAs and Co_3S_4 ultrathin NSAs are also obtained and compared, which exhibit similar morphology and structure to the FM-Co_3S_4 ultrathin NSAs (Fig. S6a, c and e). The EDX was performed for the powdered which detached from the NF substrate via long time of ultrasonic process, which further show the ratio of the total metal (Fe (or Mn) and Co) and S is close to 3:4 (Fig. S6b, d and f). Additionally, N_2 adsorption-desorption tests were examined to investigate the surface area and porous structure of the as-prepared samples. As shown in Fig. S7, the FM-Co_3S_4 ultrathin NSAs exhibit a relatively high Brunauer–Emmett–Teller (BET) surface area of 157.96 $m^2\ g^{-1}$ with an average pore size of 17.42 nm, while the BET surface area of Co_3S_4, Fe-Co_3S_4 and Mn-Co_3S_4 ultrathin NSAs is examined to be 48.94 $m^2\ g^{-1}$, 79.41 $m^2\ g^{-1}$ and 56.71 $m^2\ g^{-1}$, respectively. The larger surface area as well as mesoporous structure of the FM-Co_3S_4 ultrathin NSAs can provide more active sites, initiate rapid electrochemical reactions with electrolyte ions, and enhance the specific capacity, which are corresponding to the electrochemical performances. The doping level was controlled by precisely regulating the molar ratio of metal salts in the precursor solution (Fe: Mn: Co is 0.5: 0.5: 2 and 2: 2: 2, respectively) under identical experimental conditions, which are depicted as FM-Co_3S_4-0.5 and FM-Co_3S_4-2 ultrathin NSAs. The actual ratio of Fe, Mn, Co and S in the FM-Co_3S_4-0.5, FM-Co_3S_4 and FM-Co_3S_4-2 ultrathin NSAs were determined by EDX, which reveals the atomic ratio of Fe: Mn: Co: S is about 1.08: 0.58: 42.31: 56.03, 2.15: 1.09: 40.98: 55.78 and 4.08: 2.05: 37.92: 55.95, respectively. The ratio of the total metal (Fe, Mn and Co) and S is nearly 3:4, which can be verified the successful formation of doping rather than hybrid (Fig. S8 and Fig. 2d, inset).

The ultrathin NSAs were further investigated by TEM. Obviously, FM-Co_3S_4 ultrathin NSAs demonstrate chiffon-like nanosheets (Fig. 4a). The magnified TEM (Fig. 4b) clearly displays that wrinkled networks are constructed with ultrathin NSAs, which enables abundant active sites and facilitates the ions and electrons transfer. The high-resolution TEM (HRTEM) image shows an interplanar spacing of 0.236 nm, which is consistent with the distance of (400) plane of Co_3S_4 (Fig. 4c). In addition, the selected area electron diffraction (SAED) corresponds to the different diffraction planes of Co_3S_4 (Fig. 4d), which further proves the formation of Co_3S_4. The element distribution confirms that the Co, Mn, Fe and S elements are uniformly distributed in the ultrathin nanosheets (Fig. 4e-i). The above results confirm that the obtained product is a compound rather than a mixture of two sulfides, which also indicates the successful doping of Fe and Mn ions into the sulfide.

XPS characterization was conducted to understand the chemical compositions and electronic states of the FM-Co_3S_4 ultrathin NSAs. The high-resolution Co 2p XPS spectrum (Fig. 5a) can be deconvoluted into three doublets corresponding to Co-S (778.4 and 793.6 eV), Co^{3+} (780.5 and 796.0 eV), Co^{2+} (782.4 and 797.4 eV) [12,49]. Compared with the Fe-Co_3S_4, Mn-Co_3S_4 or Co_3S_4, the Co 2p spectrum of the FM-Co_3S_4 ultrathin NSAs shifts to higher binding energy, indicating more transferred electrons in the FM-Co_3S_4 ultrathin NSAs system. As shown in Fig. 5b, the two peaks at 161.4 eV and 162.6 eV in the S 2p spectrum correspond to the S $2p_{3/2}$ and S $2p_{1/2}$, respectively, and the other peaks near 168.4 eV are ascribed to the S—O bond on the surface [50]. The S 2p spectrum in the FM-Co_3S_4 ultrathin NSAs displays a downshift in comparison with the Fe-Co_3S_4, Mn-Co_3S_4 or Co_3S_4, suggesting the presence of electron-rich states. And the oxidation state of Fe 2p is clarified in Fig. 5c. The peak at 706.1 eV corresponds to Fe-S,

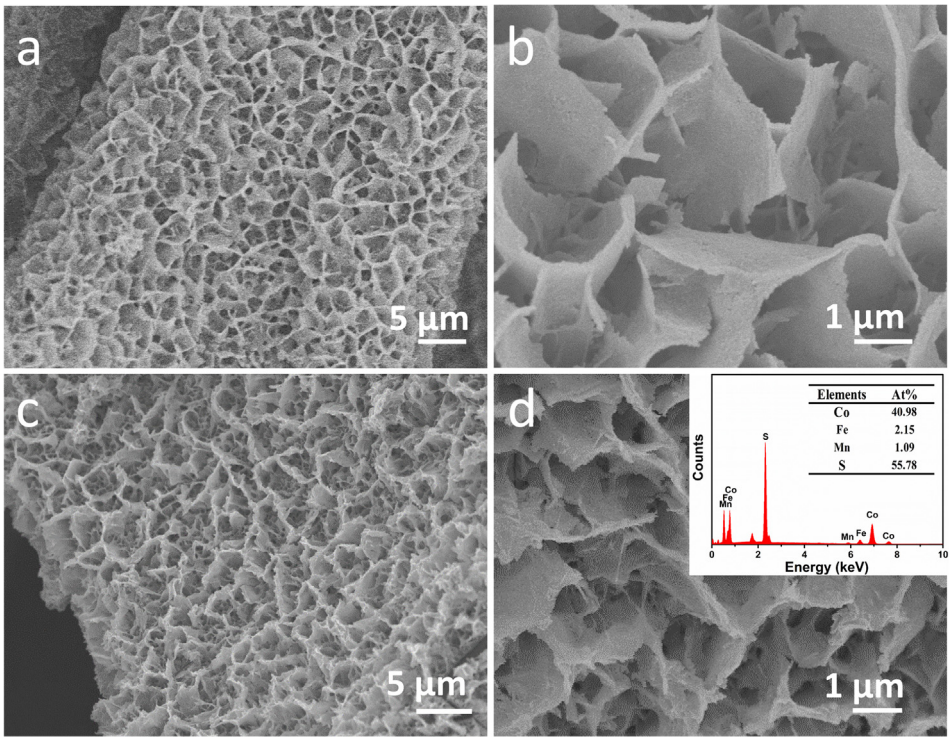

Fig. 2. SEM images of the (a, b) CoFeMn precursors, (c, d) FM-Co_3S_4 ultrathin NSAs, and the corresponding EDX spectrum (inset).

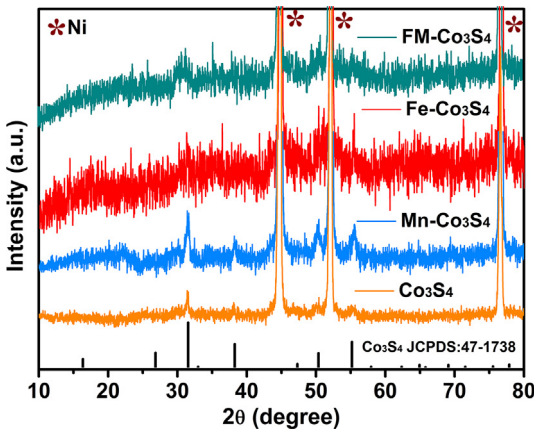

Fig. 3. XRD patterns of the as-prepared FM-Co_3S_4, Fe-Co_3S_4, Mn-Co_3S_4, and Co_3S_4 ultrathin NSAs.

and the two peaks at 711.4 eV and 714.2 eV belong to Fe $2p_{3/2}$, while the peak at 720.5 eV is ascribed to Fe $2p_{1/2}$ [51–54]. Note that the binding energies of Fe 2p in the FM-Co_3S_4 ultrathin NSAs shift negatively compared with the Fe-Co_3S_4 ultrathin NSAs, implying that the incorporated Fe species act as electron accepting sites in FM-Co_3S_4 ultrathin NSAs. The Mn 2p can be divided into three peaks, representing Mn^{2+} (638.2 eV), Mn^{3+} (641.2 eV) and Mn^{4+} (645.4 eV), respectively (Fig. 5d) [55–57]. In contrast with the Mn-Co_3S_4 ultrathin NSAs, the peaks of Mn 2p display an upshift, revealing that the Mn dopants act as electronic donors in FM-Co_3S_4 ultrathin NSAs [55]. In summary, all the above results verify that the electrons migrate from Co and Mn to Fe and S in the FM-Co_3S_4 ultrathin NSAs system, which will promote OH^- to adsorb and deprotonate/protonate, leading to superior electrochemical performance [29].

The electrochemical properties of the FM-Co_3S_4 ultrathin NSAs were tested in a three-electrode system with 2 M, 4 M and 6 M KOH aqueous electrolyte, respectively (Fig. S9). The FM-Co_3S_4 ultrathin NSAs reveal similar cyclic voltammetry (CV) profiles in the three solution and the peak areas are the largest in 6 M KOH, indicating the better capacitive performances of FM-Co_3S_4 ultrathin NSAs in higher concentration of KOH solution (Fig. S9a, c and Fig. 6a). According to the galvanostatic charge/discharge (GCD) curves (Fig. S9b, d), the specific capacities are calculated. Obviously, the specific capacities of the FM-Co_3S_4 ultrathin NSAs in 6 M KOH (390 mAh g^{-1}) electrolyte are higher than those in 4 M (280 mAh g^{-1}) and 2 M (165 mAh g^{-1}) at 5 A g^{-1}, which are corresponding to the CV curves (Fig. S9e). Moreover, KOH electrolyte with concentration of higher than 6 M has a negative effect on the NF substrate due to peeling off active materials from conductive substrate [58,59]. Therefore, 6 M KOH is used as the aqueous electrolyte in a three-electrode system. Fig. 6a compares the CV curves of the as-prepared FM-Co_3S_4 ultrathin NSAs, Mn-Co_3S_4 ultrathin NSAs, Fe-Co_3S_4 ultrathin NSAs and Co_3S_4 ultrathin NSAs recorded at a scan rate of 5 mV s^{-1} with a potential window of 0–0.5 V. Obviously, all of the CV curves show a pair of redox peaks, which can be attributed to the presence of reversible Faradaic reactions in the alkaline electrolyte. In particular, the CV curve of FM-Co_3S_4 ultrathin NSAs shows the largest enclosed area among all the as-prepared electrodes, suggesting enhanced specific capacity due to the synergistic effects of the different components in FM-Co_3S_4 ultrathin NSAs. Meanwhile, the corresponding discharging time of FM-Co_3S_4 ultrathin NSAs is the longest in the GCD at 5 A g^{-1} (Fig. 6b), which is consistent with the CV curves. In particular, the FM-Co_3S_4 ultrathin NSAs induce more active sites to promote the redox reactions more efficiently. The detailed GCD curves at different current densities are displayed in Fig. S10 and the specific capacities of the electrodes are summarized in Fig. 6c. Clearly, the FM-Co_3S_4 ultrathin NSAs deliver the specific capacity of 390 mAh g^{-1} at the current density of 5 A g^{-1}, higher than Fe-Co_3S_4 ultrathin NSAs (382 mAh g^{-1}), Mn-Co_3S_4 ultrathin NSAs (287 mAh g^{-1}),

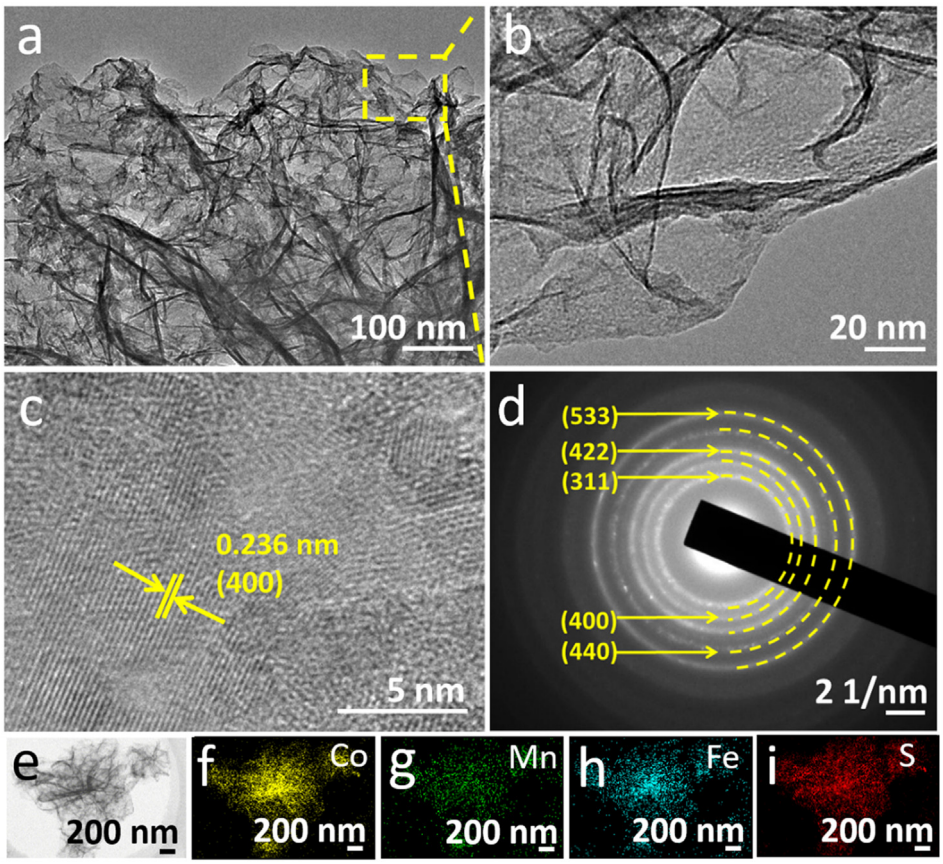

Fig. 4. (a, b) TEM images, (c) HREM image, (d) corresponding SAED pattern, and (e) STEM image of the as-prepared FM-Co_3S_4 ultrathin nanosheet, and elemental mapping images of (f) Co, (g) Mn, (h) Fe and (i) S.

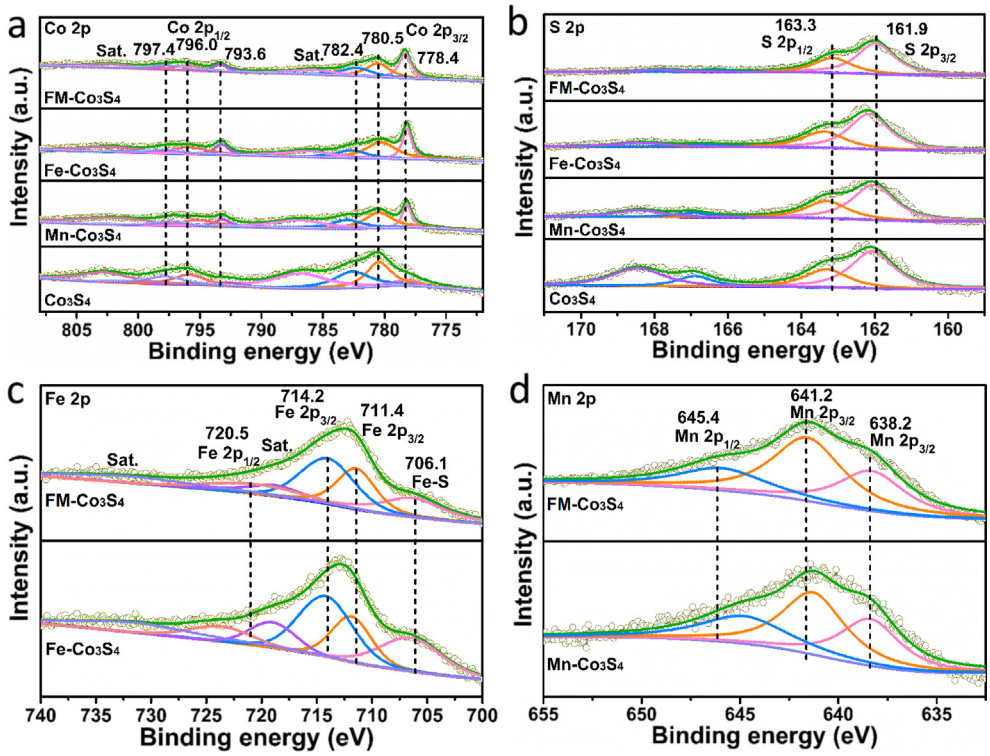

Fig. 5. XPS spectra of the as-prepared FM-Co_3S_4, Fe-Co_3S_4, Mn-Co_3S_4, and Co_3S_4 ultrathin NSAs. The high resolution XPS of (a) Co 2p, (b) S 2p, (c) Fe 2p and (d) Mn 2p.

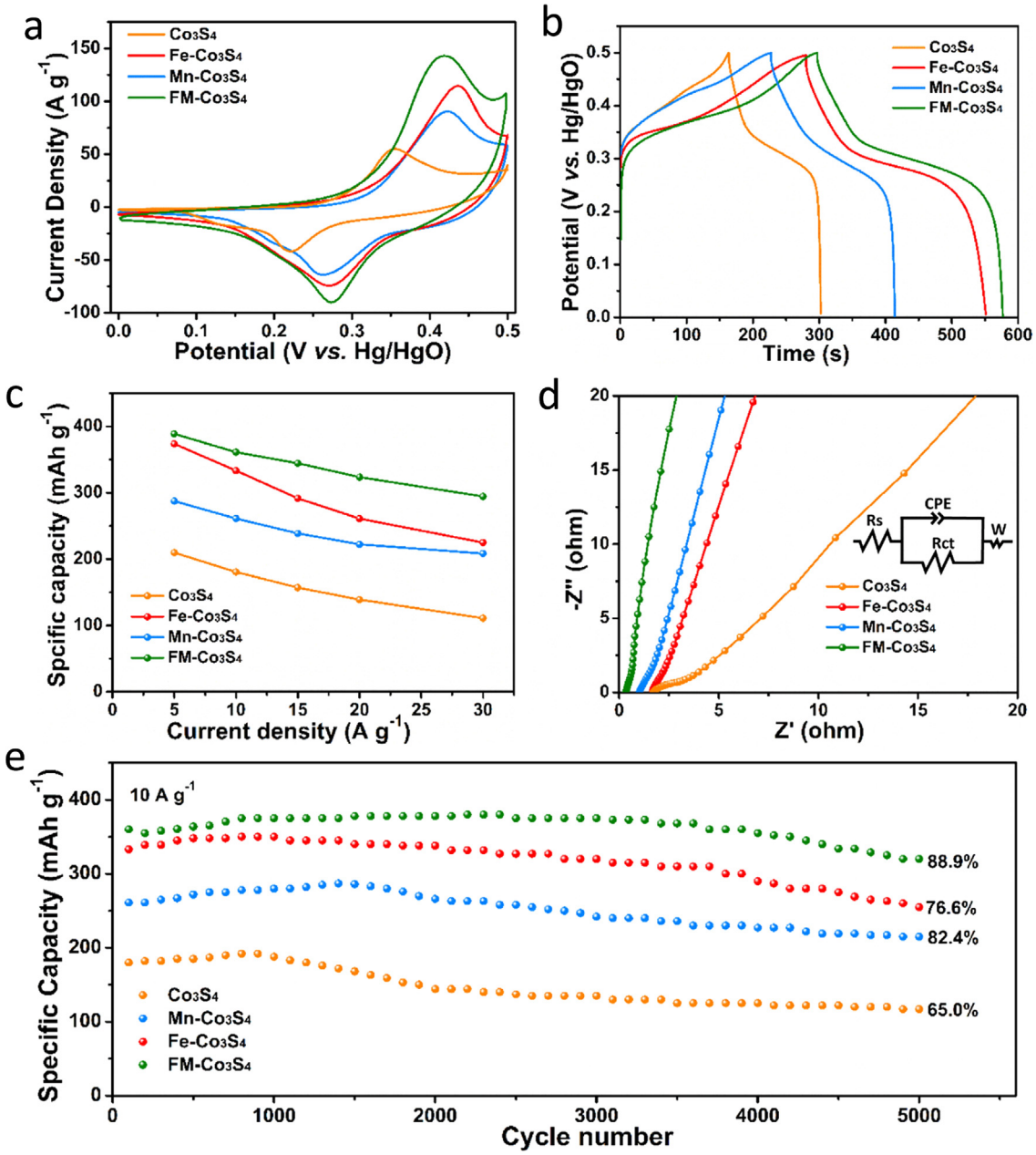

Fig. 6. Electrochemical performance of the as-prepared FM-Co_3S_4, Fe-Co_3S_4, Mn-Co_3S_4, and Co_3S_4 ultrathin NSAs: (a) CV curves at 5 mV s^{-1}, (b) GCD profiles measured at 5 A g^{-1}, (c) Specific capacities at different current density, (d) EIS spectra, (e) Cycling stability at the current density of 10 A g^{-1}.

Co_3S_4 ultrathin NSAs (215 mAh g^{-1}). Surprisingly, the specific capacity of FM-Co_3S_4 ultrathin NSAs is also superior to the reported values for Co-based electrodes (Table S1).

Ni_3S_2 nanosheets electrode is also synthesized by directly sulfurizing NF with TAA and tested in a three-electrode system with 6 M KOH aqueous electrolyte. As shown in Fig. S11, the CV curves of the Ni_3S_2 nanosheets electrode display a smallest enclosed area among all of the as-prepared electrodes. According to the GCD curves, the specific capacities are calculated. The Ni_3S_2 delivers the specific capacity of 45 mAh g^{-1} at the current density of 5 A g^{-1}, which can be ignored in comparison with the FM-Co_3S_4 ultrathin NSAs (390 mAh g^{-1}). In addition, the surface of the NF was uniformly coated with NSAs, preventing the NF from being sulfurized to some extent, which is consistent with the previously reported [60,61]. Compared with the Co_3S_4 ultrathin NSAs, the Fe-Co_3S_4 ultrathin NSAs exhibit larger CV integral area and longer discharging time, signifying the higher performance of specific capacity. And there is a gentle trend that the Mn-Co_3S_4 ultrathin NSAs display superior capacity retention to that of Co_3S_4 ultrathin NSAs, indicating improved rate capability. Therefore, it can be concluded that the Fe ions are beneficial to higher electrochemical activity and the Mn ions contribute to superior rate properties. Integrating the advantages of Fe and Mn ions, FM-Co_3S_4 ultrathin NSAs not only improve the specific capacity, but also enhance the rate capability.

Electrochemical impedance spectroscopy (EIS) measurements were carried out to evaluate the intrinsic conductivity and reaction kinetics of the as-prepared electrodes. The representative Nyquist plots of each electrode are presented in Fig. 6d, involving the equivalent series resistance (R_s), charge-transfer resistance (R_{ct}) and the diffusion resistance (R_w). The intercept of the X-axis at high frequency refers to R_s, which comprises the intrinsic resistance, contact resistance, and electrolyte resistance. The FM-

Co_3S_4 ultrathin NSAs display the lowest resistance (R_s) of 0.34 Ω among the as-prepared electrodes, indicating the highest electrical conductivity. In addition, the R_{ct} is governed by a diameter of the semicircle which controls the redox reaction kinetics. The FM-Co_3S_4 ultrathin NSAs also display the smallest R_{ct} of 0.55 Ω (0.62 Ω for Mn-Co_3S_4 ultrathin NSAs, 0.68 Ω for Fe-Co_3S_4 ultrathin NSAs, 1.15 Ω for Co_3S_4 ultrathin NSAs), implying the fastest transport in the electrochemical processes. And the straight line of the FM-Co_3S_4 ultrathin NSAs electrode is steeper than the others in the low-frequency region, suggesting the smaller diffusion resistance. Evidently, the FM-Co_3S_4 ultrathin NSAs are the favorable electrodes with enhanced conductivity and faster transfer kinetics. All these results are matched well with the CV and GCD results, which is associated with the synergistic effects of different components for the excellent electrochemical performances. Besides, the cycling stability is considered as an essential factor for practical energy storage and conversion applications. Fig. 6e compares the cycling stability of the electrodes at the current density of 10 A g^{-1}. As expected, the retention rate of the FM-Co_3S_4 ultrathin NSAs electrode maintains 88.9%, which is higher than the others, indicating the unique components of the FM-Co_3S_4 ultrathin NSAs can efficiently promote cycling stability. Specifically, the unique components of the FM-Co_3S_4 ultrathin NSAs can facilitate the transportation of electrons and ions and the ultrathin NSAs enhance the utilization of accessibility for electrolyte ion penetration. The specific capacity of the FM-Co_3S_4 ultrathin NSAs electrode shows a constant increase in the first 1200 cycles, which is due to the activation of the electrode materials. Subsequently, a stable specific capacity is well maintained until 3700 cycles and a slightly degradation is observed after 5000 cycles. The excellent stability of the FM-Co_3S_4 ultrathin NSAs electrode was further verified by the EIS results, exhibiting no obvious change after 5000 cycles (Fig. S12). To understand the outstanding electrochemical performances of the as-prepared samples, the morphology of FM-Co_3S_4 ultrathin NSAs electrode after 5000 rounds of cycling was inspected by SEM measurements, which can be observed that the morphology and structure of the ultrathin NSAs are well maintained (Fig. S13).

The detailed energy storage kinetics and mechanism were further investigated by CV characterization. The CV curves of the FM-Co_3S_4 ultrathin NSAs at different scan rates are displayed in Fig. 7a. All the curves show a pair of redox peaks, revealing the Faradaic process of battery-type electrode. Moreover, as the scan rate increases, the CV curves maintain a similar shape without distinct distortion, indicating that the FM-Co_3S_4 ultrathin NSAs electrode favors for fast redox reactions. The involved charge storage process can be described by the following reactions:

$$M_3S_4(M = Co,\ Fe,\ Mn) + 11OH^- \leftrightarrow M_3S_4(OH)_{11}(M = Co,\ Fe,\ Mn) + 11e^- \quad (6)$$

$$M_3S_4(OH)_{11}(M = Co,\ Fe,\ Mn) + 9OH^- \leftrightarrow M_3S_4O_{10}(M = Co,\ Fe,\ Mn) + 10H_2O + 9e^- \quad (7)$$

In general, the relationship between current (i) and scan rate (v) obeys a power-law as follows:

$$i = a v^b \quad (8)$$

where a and b are variables. The value of b suggests the type of current control: $b = 1$ reflects a surface-controlled process, while $b = 0.5$ implies a diffusion-controlled behavior. In the case of FM-Co_3S_4 ultrathin NSAs, the fitted b-values of the cathode and anode peaks are 0.62 and 0.63, respectively (Fig. 7b), indicating that the kinetics

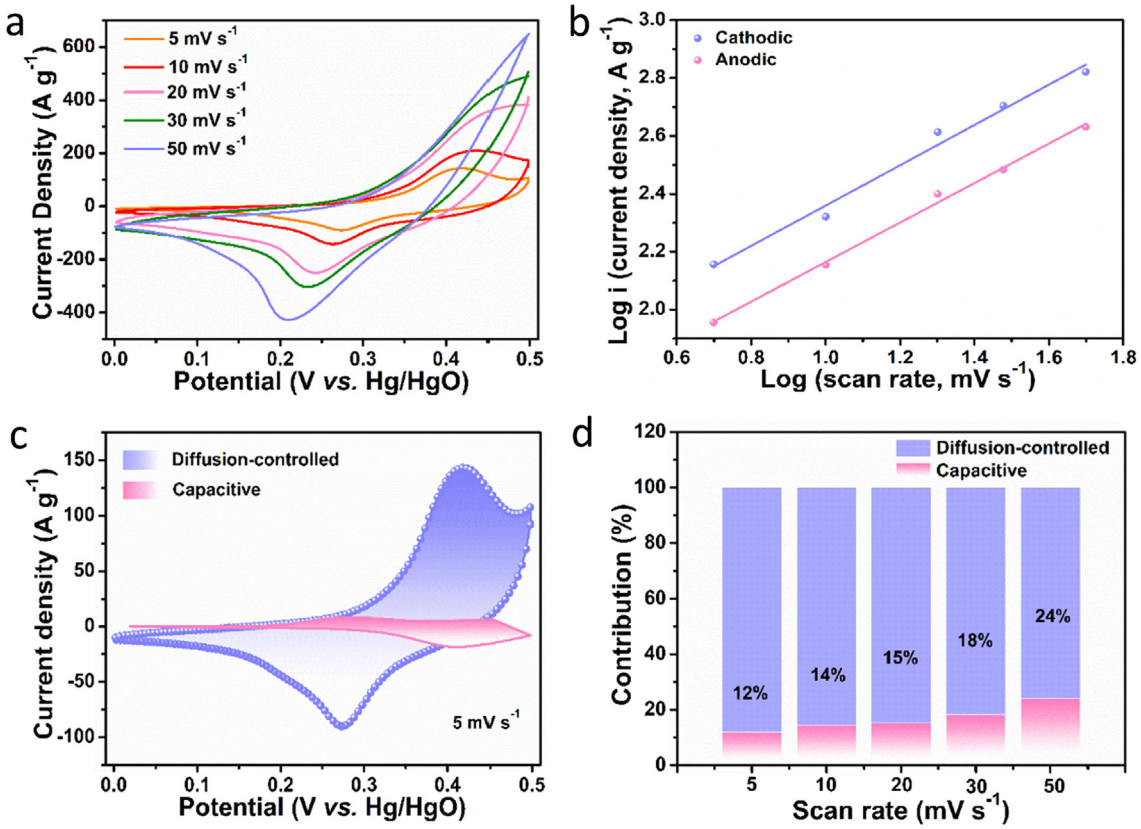

Fig. 7. (a) The CV curves of the as-prepared FM-Co_3S_4 ultrathin NSAs electrode at different scan rates, (b) The plot of log(i) versus log(v), (c) Separation of the capacitive and diffusion currents in the as-prepared FM-Co_3S_4 ultrathin NSAs electrode at a scan rate of 5 mV s^{-1}, (d) Relative contributions of the capacitive and diffusion-controlled charge storage at different scan rates.

of FM-Co_3S_4 ultrathin NSAs are regulated by a diffusion-controlled redox reaction.

The contribution of the capacitive and diffusion-controlled processes to the total capacity can be derived from the following equation:

$$i(V) = k_1 v + k_2 v^{1/2} \quad (9)$$

where i(V) is the current at a given potential V, and k_1v and $k_2v^{1/2}$ correspond to capacitive processes and diffusion-controlled effects, respectively. According to the plot i(V) with respect to $/v^{1/2}$ and $v^{1/2}$, the k_1 and k_2 constants can be determined. As shown in Fig. 7c, the capacitive contribution occupies about 12% of the entire capacity at 5 mV s^{-1}. And the contribution of the two processes at different scan rates are demonstrated in Fig. 7d. It is clear that the contribution of the diffusion-controlled process decreases with the increased scan rates, indicating the deficient diffusion time for the ions into the lattices.

The effects of doping Fe or Mn atoms on the electronic structure of Co_3S_4 ultrathin NSAs were verified via DFT calculations. In a conventional spinel Co_3S_4 cell, Co^{2+} and Co^{3+} located at tetrahedral and octahedral O^{2-} interstitial respectively (Fig. S14) [62]. Configuration of doped Co_3S_4 with Fe/Mn substituting Co at both type of interstitial sites within spinel cell were calculated, respectively. Energy comparison (Fig. S15 and Fig. S16) shows that the octahedral interstitial sites were more energetically preferable both for Fe and Mn doping. The original Co_3S_4 is a semi-conductor with an energy gap (0.58 eV as determined in current work) between valance band maximum (VBM) and conduction band minimum (CBM), as the calculated density of states (DOS) spectra shown in Fig. 8. It was found that the total density of states (TDOS) of Co_3S_4, Fe-Co_3S_4 and Mn-Co_3S_4 ultrathin NSAs near Fermi energy follows the trend: Mn-Co_3S_4 ultrathin NSAs and Fe-Co_3S_4 ultrathin NSAs > Co_3S_4 ultrathin NSAs (Fig. 8a). The band gap is reduced by different extent with doping of Fe or Mn. From the calculated partial DOS spectra in Fig. 8b-d, it can be seen that defect states are induced by the doping atoms. Especially for Mn doped Co_3S_4, the original VBM and CBM of Co_3S_4 are concatenated by the Mn induced defect states, leading to a DOS spectra of semi-metallic type ultimately. The results of DFT study indicates that doping of Fe or Mn will improve the electrical conductivity, and Mn doping has a better promotion than Fe. In addition, the potential synergetic effects of the multi-metal components in FM-Co_3S_4 ultrathin NSAs may offer more active sites to promote the reactions, which increase the number of oxidation states and accelerate the electrons transfer during the redox process. The superior electrical conductivity and better oxidation in the FM-Co_3S_4 ultrathin NSAs are favor for the final deprotonation, which potentially has a direct influence on the driving force for the charge/discharge process to enhance electrochemical performance [29,55].

Based on the above discussion, the enhanced electrochemical performances of the FM-Co_3S_4 ultrathin NSAs are ascribed to the following characteristics. Firstly, the direct attachment of the FM-Co_3S_4 ultrathin NSAs on 3D porous NF can effectively improve the conductivity of the electrode to facilitate the electron transfer. Secondly, the favorable complementarities of Co, Mn and Fe in FM-Co_3S_4 ultrathin NSAs lead to synergetic effects, providing more electroactive sites to accelerate the reactions and resulting in enhanced specific capacity and rate capability. Thirdly, the unique

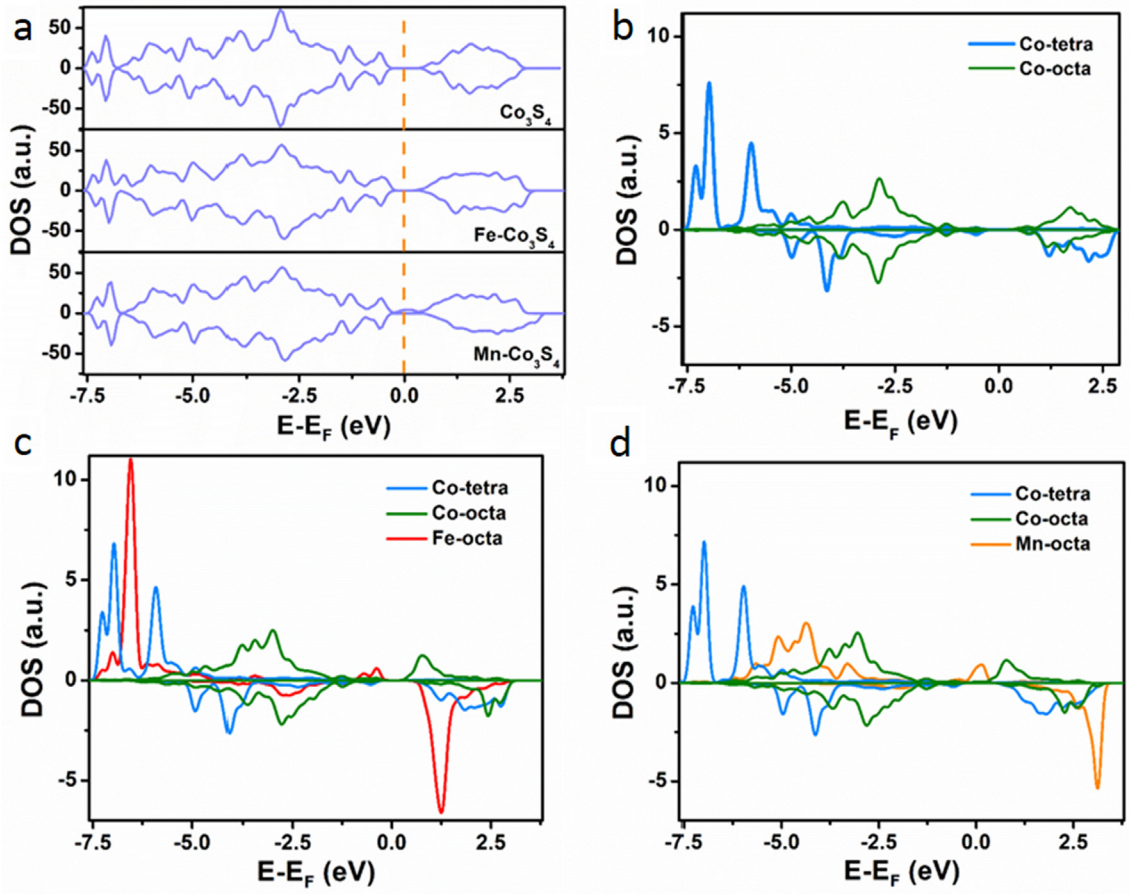

Fig. 8. Density of states (DOS) spectra of original Co_3S_4 and doped Co_3S_4 with Fe/Mn substituting Co in the octahedral interstitial sites within conventional spinel cell. (a) The total DOS of Co_3S_4, Fe-Co_3S_4 and Mn-Co_3S_4 ultrathin NSAs, (b-d) The partial DOS of Co_3S_4, Fe-Co_3S_4 and Mn-Co_3S_4 ultrathin NSAs.

ultrathin NSAs enable sufficiently accessible to the electrolyte to facilitate the redox processes.

In order to evaluate the practical application of FM-Co_3S_4 ultrathin NSAs, the corresponding HSC was assembled with FM-Co_3S_4 ultrathin NSAs and AC as the electrodes in a PVA/KOH gel electrolyte. The electrochemical performances of the AC are shown in Fig. S17, which demonstrates the specific capacitance of 223 F g^{-1} at 1 A g^{-1}. From the CV curves of the FM-Co_3S_4 ultrathin NSAs and AC at a scan rate of 5 mV s^{-1}, the stable operating voltage reaches 1.5 V (Fig. S18). Fig. 9a displays the CV curves of FM-Co_3S_4 ultrathin NSAs//AC HSC at different scan rates ranging from 5 mV s^{-1} to 100 mV s^{-1}. All the curves show a quasi-rectangular shape, indicating the superior charge match between the positive and negative electrodes. In addition, there is no distinct distortion of the CV curves at different scan rates, suggesting excellent rate capabilities. The GCD curves of FM-Co_3S_4 ultrathin NSAs//AC HSC at 1 A g^{-1} to 20 A g^{-1} display an almost symmetric behavior (Fig. 9b), demonstrating its excellent electrochemical reversibility, which can be further evidenced by the columbic efficiency according to the following equation:

$$\eta = \frac{t_d}{t_c} \tag{10}$$

where t_c and t_d are the charging and discharging time, respectively. The coulomb efficiency is close to 100% when the current density reaches 15 A g^{-1}. Based on the GCD curves, the specific capacities of FM-Co_3S_4 ultrathin NSAs//AC HSC are shown in Fig. 9c, which delivers specific capacities from 73 mAh g^{-1} at 1 A g^{-1} to 64 mAh g^{-1} at 15 A g^{-1}, revealing superior rate capability. The energy and power densities of FM-Co_3S_4 ultrathin NSAs//AC HSC are the two

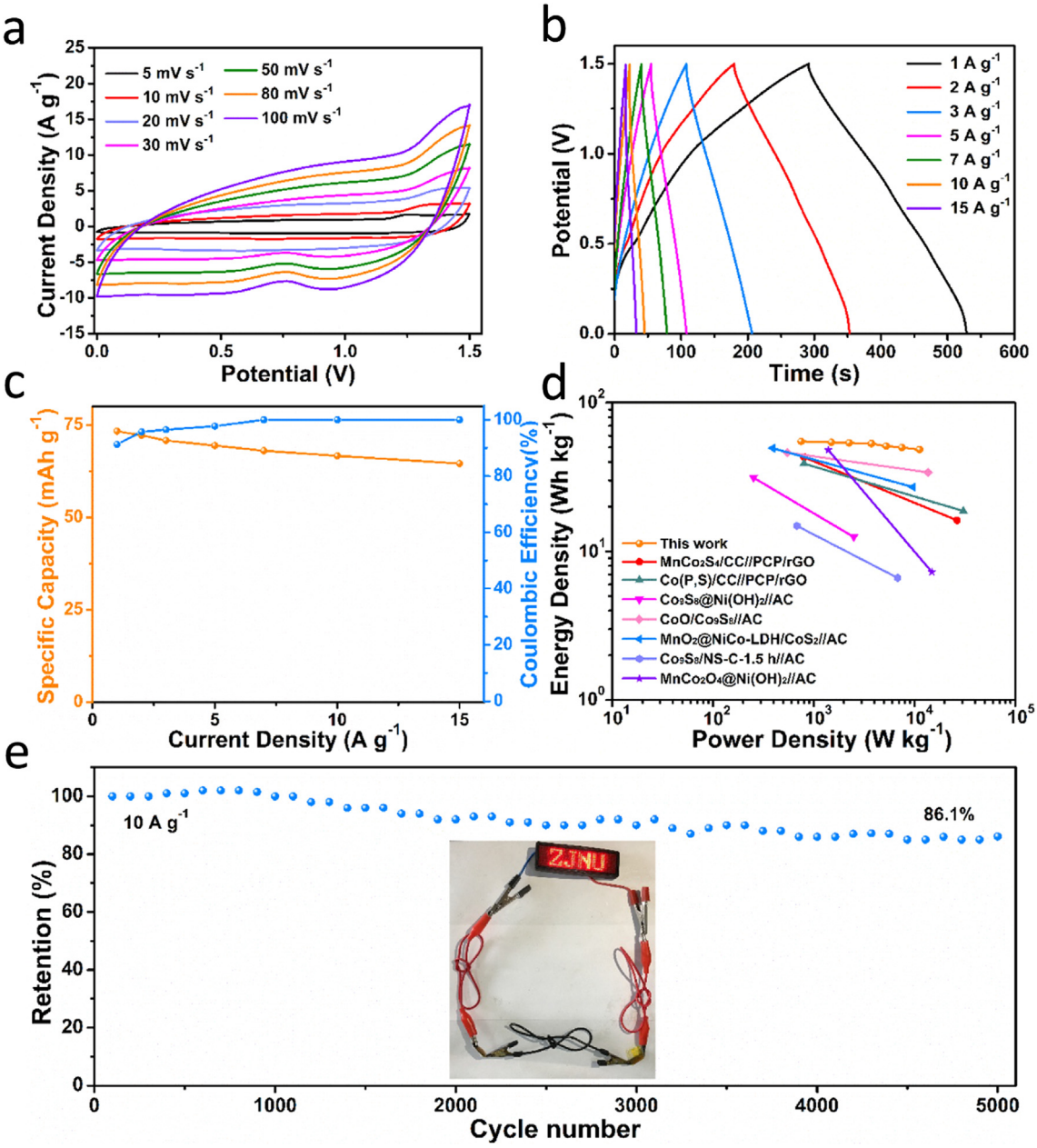

Fig. 9. Electrochemical performance of the FM-Co_3S_4 ultrathin NSAs//AC HSC. (a) CV curves at different scan rates from 5 mV s^{-1} to 100 mV s^{-1}. (b) GCD curves at different current densities from 1.0 A g^{-1} to 15 A g^{-1}. (c) Specific capacities and coulombic efficiencies at different current densities. (d) The Ragone plot compared with the state-of-the-art HSCs. (e) Cycling stability at the current density of 10 A g^{-1}. The insets of (e) shows the photographic images of LEDs lit up by two HSCs in series.

significant parameters to evaluate a HSC device, which can be calculated according to the GCD curves. As displayed in the Ragone plot (Fig. 9d), the HSC device achieves an energy density of 55 Wh kg^{-1} at the power density of 752 W kg^{-1}, and maintains 48 Wh kg^{-1} even at 11250 W kg^{-1}, which is also higher than most of recently reported HSCs, such as $MnCo_2S_4$/CC//PCP/rGO (801 W kg^{-1}, 43 Wh kg^{-1}) [63], Co (P, S)/CC//PCP/rGO (800 W kg^{-1}, 39 Wh kg^{-1}) [64], Co_9S_8@Ni$(OH)_2$//AC (252.8 W kg^{-1}, 31.35 Wh kg^{-1}) [65], CoO/Co_9S_8//AC (550 W kg^{-1}, 46.2 Wh kg^{-1}) [66], MnO_2@NiCo-LDH/CoS_2//AC (391.5 W kg^{-1}, 49.5 Wh kg^{-1}) [67], Co_9S_8/NS–C-1.5 h//AC (681.82 W kg^{-1}, 14.85 Wh kg^{-1}) [68], $MnCo_2O_4$@Ni$(OH)_2$//AC (1400 W kg^{-1}, 48 Wh kg^{-1}) [69] (Table S2). In addition, the long-term cycling stability is one of the essential factors to estimate the feasibility of the HSCs. Fig. 9e demonstrates the HSCs can retain 86.1% of the initial specific capacity after 5000 cycles at the current density of 10 A g^{-1}, suggesting excellent stability. To further evaluate the kinetics of the FM-Co_3S_4 ultrathin NSAs//AC HSC, the EIS measurements were performed before and after the 5000 cycles (Fig. S19). From the Nyquist plots, it reveals that the R_s and R_{ct} of HSCs are 1.75 Ω and 2.23 Ω, respectively. Even after the 5000 cycles, the intercept at the real axis slightly increases and a semicircle is well maintained, showing the ultrafast charge-discharge characteristics and superior cycling stability. In order to fully evaluate the practical application of the HSCs, two as-assembled HSCs in series can power light emitting diodes (LEDs) with "ZJNU" logo as illustrated in the inset of Fig. 9e. These outstanding electrochemical performances of the FM-Co_3S_4 ultrathin NSAs//AC HSC device further verifies that the FM-Co_3S_4 ultrathin NSAs are a promising candidate for the next generation of energy storage materials.

4. Conclusions

In summary, we have successfully fabricated FM-Co_3S_4 ultrathin NSAs through a facile hydrothermal method with subsequent sulfurization treatment. Benefiting from the unique structure and synergistic effects of the doped components of Fe and Mn ions, the FM-Co_3S_4 ultrathin NSAs deliver a high specific capacity of 390 mAh g^{-1} at the current density of 5 A g^{-1}, an outstanding rate capability of 76% and excellent cycling stability. The DFT calculation reveal that Mn-doped Co_3S_4 greatly improve the electrical conductivity and charge transfer, thus significantly enhance electrochemical performances. Moreover, the HSC device comprised of FM-Co_3S_4 ultrathin NSAs and AC electrodes achieves a high energy density of 55 Wh kg^{-1} at the power density of 752 W kg^{-1} and exhibits an excellent cycling stability of 86.1% retention after 5000 cycles at 10 A g^{-1}. This work demonstrates a facile strategy to engineering advanced electrode materials for next-generation energy storage applications.

CRediT authorship contribution statement

Wen Lu: Conceptualization, Formal analysis, Writing - review & editing. **Ying Yang:** Investigation, Methodology, Writing - original draft. **Tianyu Zhang:** Data curation, Methodology, Investigation. **Luankexin Ma:** Software, Validation. **Xiting Luo:** Software, Validation. **Chuanqi Huang:** Conceptualization, Methodology, Software. **Jiqiang Ning:** Writing - review & editing. **Yijun Zhong:** Formal analysis. **Yong Hu:** Conceptualization, Supervision, Funding acquisition, Writing - review & editing.

Declaration of Competing Interest

The authors declare that they have no known competing financial interests or personal relationships that could have appeared to influence the work reported in this paper.

Acknowledgements

Y. Hu acknowledges the financial support from National Natural Science Foundation of China (21671173), the Independent Designing Scientific Research Project of Zhejiang Normal University (2020ZS03) and Zhejiang Provincial Ten Thousand Talent Program (2017R52043).

Appendix A. Supplementary material

Supplementary data to this article can be found online at https://doi.org/10.1016/j.jcis.2021.01.050.

References

[1] C. Li, J. Balamurugan, N.H. Kim, J.H. Lee, Hierarchical Zn-Co-S nanowires as advanced electrodes for all solid state asymmetric supercapacitors, Adv. Energy Mater. 8 (2018) 1702014.
[2] L. Yan, Z. Xu, W. Hu, J. Ning, Y. Zhong, Y. Hu, Formation of sandwiched leaf-like CNTs-Co/$ZnCo_2O_4$@NC-CNTs nanohybrids for high-power-density rechargeable Zn-air batteries, Nano Energy 82 (2021) 105710.
[3] D. Chen, K. Jiang, T. Huang, G. Shen, Recent advances in fiber supercapacitors: materials, device configurations, and applications, Adv. Mater. 32 (2020) 1901806.
[4] B. Dunn, H. Kamath, J.M. Tarascon, Electrical energy storage for the grid: a battery of choices, Science 334 (2011) 928–935.
[5] W. Ye, H. Wang, J. Ning, Y. Zhong, Y. Hu, New types of hybrid electrolytes for supercapacitors, J. Energy Chem. 57 (2021) 219–232.
[6] Z. Meng, W. Yan, M. Zou, H. Miao, F. Ma, A.B. Patil, R. Yu, X. Yang Liu, N. Lin, Tailoring NiCoAl layered double hydroxide nanosheets for assembly of high-performance asymmetric supercapacitors, J. Colloid Interf. Sci. 583 (2021) 722–733.
[7] Y. Zhong, X. Cao, Y. Liu, L. Cui, J. Liu, Nickel cobalt manganese ternary carbonate hydroxide nanoflakes branched on cobalt carbonate hydroxide nanowire arrays as novel electrode material for supercapacitors with outstanding performance, J. Colloid Interf. Sci. 581 (2021) 11–20.
[8] H. Liu, X. Liu, S. Wang, H.K. Liu, L. Li, Transition metal based battery-type electrodes in hybrid supercapacitors: A review, Energy Storage Mater. 28 (2020) 122–145.
[9] Z. Yuan, H. Wang, J. Shen, P. Ye, J. Ning, Y. Zhong, Y. Hu, Hierarchical Cu_2S@NiCo-LDH double-shelled nanotube arrays with enhanced electrochemical performance for hybrid supercapacitors, J. Mater. Chem. A 8 (2020) 22163–22174.
[10] D.P. Dubal, O. Ayyad, V. Ruiz, P. Gomez-Romero, Hybrid energy storage: the merging of battery and supercapacitor chemistries, Chem. Soc. Rev. 44 (2015) 1777–1790.
[11] H. Lv, X. Zhang, F. Wang, G. Lv, T. Yu, M. Lv, J. Wang, Y. Zhai, J. Hu, ZIF-67-assisted construction of hollow core/shell cactus-like MnNiCo trimetal electrodes and Co, N dual-doped carbon electrodes for high-performance hybrid supercapacitors, J. Mater. Chem. A 8 (2020) 14287–14298.
[12] W. Lu, Z. Yuan, C. Xu, J. Ning, Y. Zhong, Z. Zhang, Y. Hu, Construction of mesoporous Cu-doped Co_9S_8 rectangular nanotube arrays for high energy density all-solid-state asymmetric supercapacitors, J. Mater. Chem. A 7 (2019) 5333–5343.
[13] S. Mallick, A. Mondal, C.R. Raj, Rationally designed mesoporous carbon-supported Ni–$NiWO_4$@NiS nanostructure for the fabrication of hybrid supercapacitor of long-term cycling stability, J. Power Sources 477 (2020) 229038.
[14] Q. Li, W. Lu, Z. Li, J. Ning, Y. Zhong, Y. Hu, Hierarchical MoS_2/$NiCo_2S_4$@C urchin-like hollow microspheres for asymmetric supercapacitors, Chem. Eng. J. 380 (2020) 122544.
[15] X. Zhao, L. Mao, Q. Cheng, J. Li, F. Liao, G. Yang, L. Xie, C. Zhao, L. Chen, Two-dimensional spinel structured Co-based materials for high performance supercapacitors: a critical review, Chem. Eng. J. 387 (2020) 124081.
[16] S. Li, Y. Zhang, N. Liu, C. Yu, S.J. Lee, S. Zhou, R. Fu, J. Yang, W. Guo, H. Huang, J.S. Lee, C. Wang, T.R. Kim, D. Nordlund, P. Pianetta, X. Du, J. Zhao, Y. Liu, J. Qiu, Operando revealing dynamic reconstruction of NiCo carbonate hydroxide for high-rate energy storage, Joule 4 (2020) 673–687.
[17] Z. Li, D. Zhao, C. Xu, J. Ning, Y. Zhong, Z. Zhang, Y. Wang, Y. Hu, Reduced $CoNi_2S_4$ nanosheets with enhanced conductivity for high-performance supercapacitors, Electrochim. Acta 278 (2018) 33–41.
[18] Q. Chen, J. Jin, Z. Kou, J. Jiang, Y. Fu, Z. Liu, L. Zhou, L. Mai, Cobalt-doping in hierarchical Ni_3S_2 nanorod arrays enables high areal capacitance, J. Mater. Chem. A 8 (2020) 13114–13120.
[19] E. Hu, J. Ning, D. Zhao, C. Xu, Y. Lin, Y. Zhong, Z. Zhang, Y. Wang, Y. Hu, A room-temperature postsynthetic ligand exchange strategy to construct mesoporous Fe-doped CoP hollow triangle plate arrays for efficient electrocatalytic water splitting, Small 14 (2018) 1704233.
[20] J. Jiang, Z. Li, X. He, Y. Hu, F. Li, P. Huang, C. Wang, Novel skutterudite CoP_3–Based asymmetric supercapacitor with super high energy density, Small 16 (2020) 2000180.

[21] M. Guo, J. Balamurugan, X. Li, N.H. Kim, J.H. Lee, Hierarchical 3D cobalt-doped Fe_3O_4 nanospheres@NG hybrid as an advanced anode material for high-performance asymmetric supercapacitors, Small 13 (2017) 1701275.
[22] X. Liu, W. Zang, C. Guan, L. Zhang, Y. Qian, A.M. Elshahawy, D. Zhao, S.J. Pennycook, J. Wang, Ni-doped cobalt–cobalt nitride heterostructure arrays for high-power supercapacitors, ACS Energy Lett. 3 (2018) 2462–2469.
[23] L. Cheng, Q. Zhang, M. Xu, Q. Zhai, C. Zhang, Two-for-one strategy: Three-dimensional porous Fe-doped Co_3O_4 cathode and N-doped carbon anode derived from a single bimetallic metal-organic framework for enhanced hybrid supercapacitor, J. Colloid Interf. Sci. 583 (2021) 299–309.
[24] F. Wang, K. Ma, W. Tian, J. Dong, H. Han, H. Wang, K. Deng, H. Yue, Y.X. Zhang, W. Jiang, J. Ji, P-doped $NiMoO_4$ parallel arrays anchored on cobalt carbonate hydroxide with oxygen vacancies and mass transfer channels for supercapacitors and oxygen evolution, J. Mater. Chem. A 7 (2019) 19589–19596.
[25] H.C. Chen, Y. Qin, H. Cao, X. Song, C. Huang, H. Feng, X.S. Zhao, Synthesis of amorphous nickel–cobalt–manganese hydroxides for supercapacitor-battery hybrid energy storage system, Energy Storage Mater. 17 (2019) 194–203.
[26] Z. Tang, S. Tang, Q. Li, Z. Wei, T. Zhou, Synergistic effect of microwave heating and hydrothermal methods on synthesized Ni_2CoS_4/GO for ultrahigh capacity supercapacitors, J. Colloid Interf. Sci. 582 (2021) 312–321.
[27] X. Zhou, H. Dai, X. Huang, Y. Ren, Q. Wang, W. Wang, W. Huang, X. Dong, Porous trimetallic fluoride Ni–Co–M (M= Mn, Fe, Cu, Zn) nanoprisms as electrodes for asymmetric supercapacitors, Mater. Today Energy 17 (2020) 100429.
[28] B. Huang, W. Wang, T. Pu, J. Li, C. Zhao, L. Xie, L. Chen, Rational design and facile synthesis of two-dimensional hierarchical porous $M_3V_2O_8$ (M = Co, Ni and Co–Ni) thin sheets assembled by ultrathin nanosheets as positive electrode materials for high-performance hybrid supercapacitors, Chem. Eng. J. 375 (2019) 121969.
[29] J. Li, Z. Liu, Q. Zhang, Y. Cheng, B. Zhao, S. Dai, H.H. Wu, K. Zhang, D. Ding, Y. Wu, M. Liu, M.S. Wang, Anion and cation substitution in transition-metal oxides nanosheets for high-performance hybrid supercapacitors, Nano Energy 57 (2019) 22–33.
[30] B. Huang, H. Wang, S. Liang, H. Qin, Y. Li, Z. Luo, C. Zhao, L. Xie, L. Chen, Two-dimensional porous cobalt–nickel tungstate thin sheets for high performance supercapattery, Energy Storage Mater. 32 (2020) 105–114.
[31] J. Yan, S. Li, B. Lan, Y. Wu, P.S. Lee, Rational design of nanostructured electrode materials toward multifunctional supercapacitors, Adv. Funct. Mater. 30 (2020) 1902564.
[32] C. Xu, W. Lu, L. Yan, J. Ning, C. Zheng, Y. Zhong, Z. Zhang, Y. Hu, Hierarchical molybdenum-doped cobaltous hydroxide nanotubes assembled by cross-linked porous nanosheets with efficient electronic modulation toward overall water splitting, J. Colloid Interf. Sci. 562 (2020) 400–408.
[33] C. Xu, Q. Li, J. Shen, Z. Yuan, J. Ning, Y. Zhong, Z. Zhang, Y. Hu, A facile sequential ion exchange strategy to synthesize $CoSe_2$/$FeSe_2$ double-shelled hollow nanocuboids for the highly active and stable oxygen evolution reaction, Nanoscale 11 (2019) 10738–10745.
[34] K.S. Kumar, N. Choudhary, Y. Jung, J. Thomas, Recent advances in two-dimensional nanomaterials for supercapacitor electrode applications, ACS Energy Lett. 3 (2018) 482–495.
[35] Y. Han, Y. Ge, Y. Chao, C. Wang, G.G. Wallace, Recent progress in 2D materials for flexible supercapacitors, J. Energy Chem. 27 (2018) 57–72.
[36] Y. Jiang, L. Chen, H. Zhang, Q. Zhang, W. Chen, J. Zhu, D. Song, Two-dimensional Co_3O_4 thin sheets assembled by 3D interconnected nanoflake array framework structures with enhanced supercapacitor performance derived from coordination complexes, Chem. Eng. J. 292 (2016) 1–12.
[37] Y. Da, J. Liu, L. Zhou, X. Zhu, X. Chen, L. Fu, Engineering 2D architectures toward high-performance micro-supercapacitors, Adv. Mater. 31 (2019) 1802793.
[38] F. Yi, H. Ren, J. Shan, X. Sun, D. Wei, Z. Liu, Wearable energy sources based on 2D materials, Chem. Soc. Rev. 47 (2018) 3152–3188.
[39] J. Zhu, B. Huang, C. Zhao, H. Xu, S. Wang, Y. Chen, L. Xie, L. Chen, Benzoic acid-assisted substrate-free synthesis of ultrathin nanosheets assembled two-dimensional porous Co_3O_4 thin sheets with 3D hierarchical micro-/nano-structures and enhanced performance as battery-type materials for supercapacitors, Electrochim. Acta 313 (2019) 194–204.
[40] B. Huang, W. Wang, T. Pu, J. Li, J. Zhu, C. Zhao, L. Xie, L. Chen, Two-dimensional porous (Co, Ni)-based monometallic hydroxides and bimetallic layered double hydroxides thin sheets with honeycomb-like nanostructure as positive electrode for high-performance hybrid supercapacitors, J. Colloid Interf. Sci. 532 (2018) 630–640.
[41] J. Zhu, D. Song, T. Pu, J. Li, B. Huang, W. Wang, C. Zhao, L. Xie, L. Chen, Two-dimensional porous $ZnCo_2O_4$ thin sheets assembled by 3D nanoflake array with enhanced performance for aqueous asymmetric supercapacitor, Chem. Eng. J. 336 (2018) 679–689.
[42] Y. Du, G. Li, M. Chen, X. Yang, L. Ye, X. Liu, L. Zhao, Hollow nickel-cobalt-manganese hydroxide polyhedra via MOF templates for high-performance quasi-solid-state supercapacitor, Chem. Eng. J. 378 (2019) 12210.
[43] H. Chen, L. Hu, Y. Yan, R. Che, M. Chen, L. Wu, One-step fabrication of ultrathin porous nickel hydroxide-manganese dioxide hybrid nanosheets for supercapacitor electrodes with excellent capacitive performance, Adv. Energy Mater. 3 (2013) 1636–1646.
[44] C. Tang, R. Zhang, W. Lu, L. He, X. Jiang, A.M. Asiri, X. Sun, Fe-doped CoP nanoarray: a monolithic multifunctional catalyst for highly efficient hydrogen generation, Adv. Mater. 29 (2017) 1602441.
[45] W. Zhu, K. Tang, J. Li, W. Liu, X. Niu, G. Zhao, X. Ma, Z. Liu, H. Wei, Y. Yang, The effect of copper species in copper-ceria catalysts: structure evolution and enhanced performance in CO oxidation, RSC Adv. 6 (2016) 46966–46971.
[46] Z. Zhang, Y. Huang, X. Liu, C. Chen, Z. Xu, P. Liu, Zeolitic imidazolate frameworks derived ZnS/Co_3S_4 composite nanoparticles doping on polyhedral carbon framework for efficient lithium/sodium storage anode materials, Carbon 157 (2020) 244–254.
[47] H. Wang, Y. Yang, Q. Li, W. Lu, J. Ning, Y. Zhong, Z. Zhang, Y. Hu, Molecule-assisted modulation of the high-valence Co^{3+} in 3D honeycomb-like Co_xS_y networks for high-performance solid-state asymmetric supercapacitors, Sci. China Mater. (2020), https://doi.org/10.1007/s40843-020-1476-2.
[48] Y. Wu, H. Yang, Y. Yang, H. Pu, W. Meng, R. Gao, D. Zhao, SnS_2/Co_3S_4 hollow nanocubes anchored on S-doped graphene for ultrafast and stable Na-ion storage, Small 15 (2019) 1903873.
[49] Q. Lu, J. Yu, X. Zou, K. Liao, P. Tan, W. Zhou, M. Ni, Z. Shao, Self-catalyzed growth of Co, N-codoped CNTs on carbon-encased CoS_x surface: a noble-metal-free bifunctional oxygen electrocatalyst for flexible solid Zn–air batteries, Adv. Funct. Mater. 29 (2019) 1904481.
[50] W. Lu, J. Shen, P. Zhang, Y. Zhong, Y. Hu, X.W. Lou, Construction of CoO/Co-Cu-S hierarchical tubular heterostructures for hybrid supercapacitors, Angew. Chem. Int. Ed. 58 (2019) 15441–15447.
[51] A.A. Eissa, S.G. Peera, N.H. Kim, J.H. Lee, g-C_3N_4 templated synthesis of Fe_3C@NSC electrocatalyst enriched with Fe–N_x active sites for efficient oxygen reduction reaction, J. Mater. Chem. A 7 (2019) 16920–16936.
[52] C. Xuan, W. Lei, J. Wang, T. Zhao, C. Lai, Y. Zhu, Y. Sun, D. Wang, Sea urchin-like Ni–Fe sulfide architectures as efficient electrocatalysts for the oxygen evolution reaction, J. Mater. Chem. A 7 (2019) 12350–12357.
[53] W. Wei, S. Yang, H. Zhou, I. Lieberwirth, X. Feng, K. Müllen, 3D graphene foams cross-linked with pre-encapsulated Fe_3O_4 nanospheres for enhanced lithium storage, Adv. Mater. 25 (2013) 2909–2914.
[54] Y. Wang, G. Wang, W. Deng, J. Han, L. Qin, B. Zhao, L. Guo, F. Xing, Study on the structure-activity relationship of Fe-Mn oxide catalysts for chlorobenzene catalytic combustion, Chem. Eng. J. 395 (2020) 125172.
[55] L. Yan, Y. Ren, X. Zhang, Y. Sun, J. Ning, Y. Zhong, B. Teng, Y. Hu, Electronic modulation of composite electrocatalysts derived from layered NiFeMn triple hydroxide nanosheets for boosted overall water splitting, Nanoscale 11 (2019) 20797–20808.
[56] S. Cai, D. Zhang, L. Shi, J. Xu, L. Zhang, L. Huang, H. Li, J. Zhang, Porous Ni–Mn oxide nanosheets in situ formed on nickel foam as 3D hierarchical monolith de-NO_x catalysts, Nanoscale 6 (2014) 7346–7353.
[57] X. Guo, T. Zheng, G. Ji, N. Hu, C. Xu, Y. Zhang, Core/shell design of efficient electrocatalysts based on $NiCo_2O_4$ nanowires and NiMn LDH nanosheets for rechargeable zinc–air batteries, J. Mater. Chem. A 6 (2018) 10243–10252.
[58] X. Lang, H. Zhang, X. Xue, C. Li, X. Sun, Z. Liu, H. Nan, X. Hu, H. Tian, Rational design of $La_{0.85}Sr_{0.15}MnO_3$@$NiCo_2O_4$ core–shell architecture supported on Ni foam for high performance supercapacitors, J. Power Sources 402 (2018) 213–220.
[59] W. Jiang, F. Hu, Q. Yan, X. Wu, Investigation on electrochemical behaviors of $NiCo_2O_4$ battery-type supercapacitor electrodes: the role of an aqueous electrolyte, Inorg. Chem. Front. 4 (2017) 1642–1648.
[60] C. Li, J. Balamurugan, N.H. Kim, J.H. Lee, Hierarchical Zn–Co–S nanowires as advanced electrodes for all solid state asymmetric supercapacitors, Adv. Energy Mater. 8 (2018) 1702014.
[61] C. Li, J. Balamurugan, D.C. Nguyen, N.H. Kim, J.H. Lee, Hierarchical manganese–nickel sulfide nanosheet arrays as an advanced electrode for all-solid-state asymmetric supercapacitors, ACS Appl. Math. Interf. 12 (2020) 21505–21514.
[62] J. Chen, X. Wu, A. Selloni, Electronic structure and bonding properties of cobalt oxide in the spinel structure, Phys. Rev. B 83 (2011) 245204.
[63] A.M. Elshahawy, X. Li, H. Zhang, Y. Hu, K.H. Ho, C. Guan, J. Wang, Controllable $MnCo_2S_4$ nanostructures for high performance hybrid supercapacitors, J. Mater. Chem. A 5 (2017) 7494–7506.
[64] A.M. Elshahawy, C. Guan, X. Li, H. Zhang, Y. Hu, H. Wu, S.J. Pennycook, J. Wang, Sulfur-doped cobalt phosphide nanotube arrays for highly stable hybrid supercapacitor, Nano Energy 39 (2017) 162–171.
[65] F. Zhu, M. Yan, Y. Liu, H. Shen, Y. Lei, W. Shi, Hexagonal prism-like hierarchical Co_9S_8@$Ni(OH)_2$ core–shell nanotubes on carbon fibers for high-performance asymmetric supercapacitors, J. Mater. Chem. A 5 (2017) 22782–22789.
[66] Y. Wang, T. Zhu, Y. Zhang, X. Kong, S. Liang, G. Cao, A. Pan, Rational design of multi-shelled CoO/Co_9S_8 hollow microspheres for high-performance hybrid supercapacitors, J. Mater. Chem. A 5 (2017) 18448–18456.
[67] X. Wang, F. Huang, F. Rong, P. He, R. Que, S.P. Jiang, Unique MOF-derived hierarchical MnO_2 nanotubes@NiCo-LDH/CoS_2 nanocage materials as high performance supercapacitors, J. Mater. Chem. A 7 (2019) 12018–12028.
[68] S. Zhang, D. Li, S. Chen, X. Yang, X. Zhao, Q. Zhao, S. Komarneni, D. Yang, Highly stable supercapacitors with MOF-derived Co_9S_8/carbon electrodes for high rate electrochemical energy storage, J. Mater. Chem. A 5 (2017) 12453–12461.
[69] Y. Zhao, L. Hu, S. Zhao, L. Wu, Preparation of $MnCo_2O_4$@$Ni(OH)_2$ Core-Shell flowers for asymmetric supercapacitor materials with ultrahigh specific capacitance, Adv. Funct. Mater. 26 (2016) 4085–4093.